

Photon-dark photon oscillation in M87 and Crab Nebula environments

Tanmay Kumar Poddar^{1a}, Sourov Roy^{2b}, and Pratick Sarkar^{2c}

¹ *Institute for Particle Physics Phenomenology (IPPP),*

Department of Physics, Durham University,

Durham DH1 3LE, United Kingdom and

² *School of Physical Sciences, Indian Association for the Cultivation of Science,
2A & 2B Raja S.C. Mullick Road, Kolkata-700032, India*

Abstract

Compact astrophysical systems such as neutron stars and black holes provide powerful laboratories for testing feebly coupled dark photons (DPs). We investigate light DPs kinetically mixed with the visible photon that need not be the dark matter, focusing on resonant photon-DP oscillations in magnetized, modeled plasma environments. We show that realistic non-monotonic plasma density profiles generically enhance resonant conversion relative to monotonic models, leading to substantially stronger constraints on the photon-DP kinetic mixing parameter (ϵ). Using spectral data from the supermassive black hole (SMBH) M87*, extending to the LOFAR band, we derive a bound $\epsilon \simeq 7 \times 10^{-6}$ at the DP mass $m_{A'} \simeq 5 \times 10^{-7}$ eV for oscillation distance $3r_{\text{ph}}$, where r_{ph} denotes the photon sphere radius. From the Crab pulsar-wind Nebula, we obtain an even stronger constraint, $\epsilon \simeq 8 \times 10^{-7}$ at $m_{A'} \simeq 4 \times 10^{-9}$ eV for oscillation baselines of order 10^3 km, surpassing existing astrophysical limits in realistic plasma backgrounds. While laboratory and cosmological bounds remain slightly stronger at comparable masses, observation of compact objects with larger surface magnetic fields and measurements of photon spectra at lower frequencies would enhance the limits on the photon-DP coupling by orders of magnitude.

^a tanmay.k.poddar@durham.ac.uk

^b tpsr@iacs.res.in

^c spsps2523@iacs.res.in

I. INTRODUCTION

Compact objects such as black holes (BHs) and neutron stars (NSs) provide unique cosmic laboratories for exploring physics beyond the Standard Model (SM) through their observed electromagnetic (EM) emission spectra [1, 2]. Compared to conventional terrestrial experiments, these astrophysical systems offer several advantages in probing ultralight beyond-SM degrees of freedom, such as dark photons (DPs) that could constitute a fraction of the dark matter (DM) in the Universe. The extreme conditions in and around compact stars characterized by intense magnetic fields, high particle densities, and large spatial extensions significantly enhance the interaction probability of such light particles with the surrounding plasma and radiation. Moreover, their long-lived and continuously monitored emission allows for the accumulation of small effects over extended timescales. Consequently, compact stars act as natural, large-volume detectors that provide a powerful and complementary avenue to Earth-based direct detection experiments in the search for light dark sector particles.

In contrast to axions or scalar fields [3–7], DPs represent a spin-1 extension of the SM, interacting with ordinary photons through kinetic mixing [8]. The vector nature of DPs leads to distinct phenomenology. Unlike photon-axion oscillations, which require a non-zero $\mathbf{E} \cdot \mathbf{B}$ background from the stellar electric (**E**) and magnetic (**B**) fields, photon-DP conversion arises through plasma-induced resonances that naturally occur in compact-star magnetospheres. Moreover, the accessible mass range and coupling structure of DPs are less model-dependent than those of axions, allowing a broader exploration of hidden-sector parameter space. Astrophysical environments such as NSs, BHs and magnetars, with their magnetic fields and dense plasmas, therefore offer robust means to probe DP couplings, providing powerful and complementary constraints to those obtained from terrestrial axion and scalar searches.

DPs can be produced through a variety of mechanisms depending on the ambient plasma conditions and the kinetic-mixing strength (ϵ) with the SM photon. In stellar and magnetized environments, their production primarily proceeds via photon-DP oscillations in regions where the effective plasma mass of the photon, ω_p , approaches the DP mass, $m_{A'}$, leading to resonant conversion [9]. In dense or hot plasmas, additional non-resonant production channels arise from processes such as plasmon decay [10, 11], Compton-like scattering [12, 13], and bremsstrahlung emission [14] involving charged particles. The correspond-

ing emission rate depends sensitively on the local temperature, density, and magnetic field strength, which determine both the photon dispersion relation and the effective mixing angle. In compact stars, the combination of high plasma frequency and intense magnetic fields enhances these production channels, allowing even feeble kinetic mixing parameters to leave observable imprints on the emitted EM spectra or energy-loss rates. Consequently, DP production in such environments provides an astrophysically powerful probe of hidden-sector physics.

In this work, we investigate photon-DP oscillations in compact-star (BH and NS) environments within a model-agnostic framework. DPs generally arise from an additional Abelian gauge symmetry, $U(1)_D$, that kinetically mixes with the SM photon through the term $(\epsilon/2)F_{\mu\nu}F'^{\mu\nu}$, where $F_{\mu\nu}$ ($F'_{\mu\nu}$) denotes the EM (dark EM) field strength tensor [15–21]. Their mass can originate either from a Stückelberg mechanism or from a dark-Higgs field acquiring a vacuum expectation value. Depending on the mixing strength and thermal history of the Universe, DPs may be produced through freeze-in [22], freeze-out [23], or misalignment processes [24], potentially contributing to the DM density. In compact stars, the efficiency of photon-DP conversion is governed by the interplay between the DP mass $m_{A'}$ and the local plasma frequency $\omega_p(r)$. When the resonance condition $m_{A'} \simeq \omega_p(r)$ is met within the stellar magnetosphere or interior, part of the EM flux can convert into DPs, giving rise to observable effects such as spectral distortions [25], spin correlation [26], or excess cooling signatures [27].

The effective mass of a photon can vary spatially or temporally as it propagates through the environment of a compact star [28, 29]. Similarly, the DP may acquire medium-dependent corrections to its effective mass from interactions with background dark-sector particles charged under $U(1)_D$ [30–32]. The non-adiabatic photon-DP transition probability near a level crossing—the spatial point where the photon plasma mass equals the DP mass, leading to resonant mixing—is typically evaluated using the Landau-Zener (LZ) formalism [33, 34], whose leading order contribution follows from the stationary-phase approximation. The LZ probability is intrinsically oscillatory, making high-precision numerical evaluation challenging. However, close to resonance points, the oscillations become slow, and the relative phase between successive resonances can be averaged out, yielding a dominant stationary-phase transition probability. Nevertheless, it has been shown in [35] that the LZ approximation breaks down when the resonant conversion occurs near a local extremum

of the in-medium SM photon mass. Such situations arise naturally when the background particle density of the compact star plasma varies non-monotonically in space or time along the photon trajectory.

Existing constraints on the photon-DP kinetic mixing parameter arise from a wide range of laboratory, astrophysical, and cosmological observations [36, 37]. Laboratory limits include precision tests of Coulomb’s law and bounds on the photon mass [38, 39], and light-shining-through-walls or helioscope experiments [40–42]. Additional constraints are derived from BH superradiance [43], reactor neutrino data [44], and cosmological observations such as COBE/FIRAS [45], Planck+unWISE [46], as well as from astrophysical systems including the Sun [47], planets [48, 49], NSs [50], and red giants [51]. Some of these bounds assume that DPs constitute the DM [52–55]. Other related constraints and projected sensitivities to the kinetic-mixing parameter have also been discussed in [36, 37].

In this work, we derive new limits on the photon-DP kinetic-mixing parameter by analyzing low-frequency radio observations of the galaxy Messier 87 (M87) obtained with the Low Frequency ARray (LOFAR) telescope [56, 57] in the $10 - 1000$ MHz range, considering different plasma density profiles around its supermassive black hole (SMBH) [58–66]. We further explore the global spectral energy distribution (SED) of the Crab Nebula [67] in the 1-100 GHz frequency range, incorporating polarization data from the Planck satellite [68–70], to place complementary constraints. Because the background plasma potential in these environments can exhibit non-monotonic variations, the photon-DP conversion probability may receive significant corrections relative to existing estimates. Such effects can also be generalized to other two-state oscillation systems, including photon-axion and neutrino flavor oscillations in matter. Importantly, the bounds obtained in this study do not rely on the assumption that the DP constitutes the DM component.

The paper is structured as follows. In Section. II, we review the formalism of photon-DP conversion in both monotonic and non-monotonic background potentials relevant to compact star environments. Section. III presents the electron density profile around M87 and photon-DP oscillation probabilities in monotonic and non-monotonic potentials. In Section. IV, we perform a similar analysis using the spectral energy distribution of the Crab Nebula to obtain conversion probability. In Section. V, we summarize the methodology for the spectral modeling and the data analysis. Section. VI discusses about the limits obtained on photon-DP kinetic mixing. Finally, Section. VII summarizes our findings and outlines

potential implications for future studies.

Throughout this paper, we adopt natural units with $c = \hbar = 1$, where c denotes the speed of light in vacuum and \hbar is the reduced Planck constant, unless stated otherwise.

II. PHOTON-DARK PHOTON OSCILLATION PROBABILITY FOR MONOTONIC AND NON-MONOTONIC POTENTIALS

In this section, we briefly review the photon-DP oscillation formalism and derive the standard LZ transition probability for a monotonic background potential [33, 34], as well as the corresponding expression for a non-monotonic potential when the resonant conversion occurs near a local extremum of the in-medium photon mass [35]. These probability formulations will be used in the subsequent analysis to study photon-DP conversion in compact star environments.

The low energy effective Lagrangian describing the photon and DP fields coupled through kinetic mixing is given by

$$\mathcal{L} = -\frac{1}{4}F_{\mu\nu}F^{\mu\nu} - \frac{1}{4}F'_{\mu\nu}F'^{\mu\nu} + \frac{\epsilon}{2}F_{\mu\nu}F'^{\mu\nu} + \frac{1}{2}m_{A'}^2A'_\mu A'^\mu + j^\mu A_\mu, \quad (1)$$

where A_μ and A'_μ denote the SM photon and DP fields, respectively, and j_μ is the SM-EM current. The kinetic-mixing term can be eliminated by transforming A_μ to the interaction basis

$$A^\mu \equiv \begin{pmatrix} A_a^\mu \\ A_n^\mu \end{pmatrix} \quad (2)$$

in which the sterile state A_n^μ does not couple directly to the SM current, while the mass matrix becomes non-diagonal, allowing for oscillations between the active A_a^μ and sterile A_n^μ photon states. Accordingly the fields transform as $A_a^\mu \rightarrow A_\mu$ and $A_n^\mu \rightarrow A'_\mu - \epsilon A_\mu$.

In the relativistic limit, $\omega \simeq k \gg m_\gamma, m_{A'}$, where ω and k denote the frequency and wave number of the photon field A_μ and the photon acquires an effective mass m_γ due to its propagation through a plasma of free charges and EM fields, the evolution of the transverse modes of the photon-DP system can be described by a two-state Schrödinger-like equation,

$$i\partial_z A = HA, \quad H = H_0 + H_1, \quad (3)$$

where the Hamiltonian components are given by

$$H_0(z) = \begin{pmatrix} \omega + \delta(z) & 0 \\ 0 & \omega + \delta_{A'} \end{pmatrix}, \quad H_1 = \begin{pmatrix} 0 & \epsilon\delta_{A'} \\ \epsilon\delta_{A'} & 0 \end{pmatrix}, \quad (4)$$

with $\delta(z) = -m_\gamma^2(z)/2\omega$ and $\delta_{A'} = -m_{A'}^2/2\omega$. Since $H_0(z)$ is diagonal for all z , it commutes with itself at unequal spatial points, i.e. $[H_0(z), H_0(z')] = 0$.

The interaction picture Hamiltonian is

$$H_{\text{int}}(z) = U^\dagger(z)H_1(z)U(z) = \epsilon\delta_{A'} \begin{pmatrix} 0 & e^{i\varphi(z)} \\ e^{-i\varphi(z)} & 0 \end{pmatrix}, \quad (5)$$

where

$$U(z) = \exp \left[-i \int_{z_0}^z dz' H_0(z') \right] = \begin{pmatrix} e^{-i \int (\omega + \delta) dz'} & 0 \\ 0 & e^{-i \int (\omega + \delta_{A'}) dz'} \end{pmatrix}; \quad \varphi(z) = \int_{z_0}^z dz' \delta_{\text{osc}}(z'), \quad (6)$$

with $\delta_{\text{osc}} = \delta(z) - \delta_{A'}$, where z_0 is the point where we fix our initial condition $A(z_0) = A_{\text{int}}(z_0)$.

Therefore, in the Schrödinger picture, the evolution equation of A_μ becomes

$$A(z) = e^{-i \int_{z_0}^z dz' H_0(z')} e^{-i \int_{z_0}^z dz' H_{\text{int}}(z')} A(z_0). \quad (7)$$

Therefore, in the limit $\epsilon \ll 1$, Eq. 7 becomes

$$A(z) = e^{-i \int (\omega + \delta(z)) dz'} \begin{pmatrix} 1 & -i\epsilon\mathcal{C}_+ \\ -i\epsilon\mathcal{C}_- e^{i\varphi(z)} & e^{i\varphi(z)} \end{pmatrix} A(z_0) + \mathcal{O}(\epsilon^2). \quad (8)$$

where

$$\mathcal{C}_{+(-)} = \int_{z_0}^z dz' e^{+(-)i\varphi(z')} \delta_{A'}(z'). \quad (9)$$

Thus, if the initial state at z_0 is purely active i.e., $A(z_0) = (1 \ 0)^T$, then the active to sterile transition amplitude is

$$\mathcal{A}_{a \rightarrow n}(z) = -i\epsilon\mathcal{C}_- e^{i\varphi(z)} = -i\epsilon e^{i\varphi(z)} \int_{z_0}^z dz' \delta_{A'}(z') e^{-i\varphi(z')}. \quad (10)$$

As, δ_{osc} is real, φ is real and hence $\mathcal{C}_- = \mathcal{C}_+^*$. Therefore, the active to sterile oscillation probability transition is

$$P_{a \rightarrow n} = |\mathcal{A}_{a \rightarrow n}|^2 = \epsilon^2 \left| \int_{z_0}^z dz' \delta_{A'}(z') e^{i\varphi(z')} \right|^2 + \mathcal{O}(\epsilon^3). \quad (11)$$

If the initial state is sterile i.e., $A(z_0) = (0 \ 1)^T$, then

$$\mathcal{A}_{n \rightarrow a}(z) = -i\epsilon\mathcal{C}_+, \quad P_{n \rightarrow a} = \epsilon^2|\mathcal{C}_+|^2 = \epsilon^2|\mathcal{C}_-|^2 + \mathcal{O}(\epsilon^3) = P_{a \rightarrow n}. \quad (12)$$

In the following, we consider three limiting cases: photon propagation in vacuum, the LZ transition probability for a monotonic potential derived under the stationary-phase approximation, and the non-monotonic potential case where the LZ approximation ceases to be valid.

A. Vacuum case:

In the case of photon propagation in vacuum, where no plasma effects are present, the photon acquires no effective mass, i.e., $\delta(z) = 0$ while $\delta_{A'}$ is constant. Consequently, the phase becomes $\varphi(z') = -\delta_{A'}(z' - z_0)$. Therefore, we can write

$$\int_{z_0}^z dz' \delta_{A'} e^{i\varphi(z')} = \frac{1 - e^{-i\delta_{A'} L}}{i}, \quad (13)$$

with $L = z - z_0$. Thus, the active-sterile oscillation probability becomes

$$P_{a \leftrightarrow n} = 4\epsilon^2 \sin^2 \left(\frac{\delta_{A'} L}{2} \right) + \mathcal{O}(\epsilon^3). \quad (14)$$

For a constant background, the active-sterile oscillation probability beyond resonance can be obtained as

$$P_{a \leftrightarrow n} = \sin^2(2\theta_m) \sin^2 \left(\delta_m L \right), \quad (15)$$

where

$$\tan 2\theta_m = \frac{2\epsilon\delta_{A'}}{\delta_{A'} - \delta(z)}, \quad \delta_m = \sqrt{\epsilon^2\delta_{A'}^2 + \frac{(\delta_{A'} - \delta(z))^2}{4}}. \quad (16)$$

In the limit $\epsilon \ll 1$ and $\delta = 0$, Eq. 15 reduces to Eq. 14.

B. Stationary-phase approximation and Landau-Zener formula

When the phase $\varphi(z)$ is highly oscillatory, the conversion probability integral can be evaluated using the stationary-phase approximation, as the probability varies slowly near the stationary points z_n satisfying $\varphi'(z_n) = 0$. These correspond to the resonance condition $\delta(z_n) = \delta_{A'}$. Expanding the phase around each stationary point yields

$$\varphi(z) \simeq \varphi(z_n) + \frac{1}{2}\varphi''(z_n)(z - z_n)^2, \quad \delta_{A'}(z) \simeq \delta_{A'}(z_n), \quad (17)$$

and each saddle contributes

$$\int dz \delta_{A'}(z) e^{i\varphi(z)} \simeq \sum_n \delta_{A'}(z_n) e^{i\varphi(z_n)} \sqrt{\frac{2\pi}{|\varphi''(z_n)|}} e^{i\frac{\pi}{4}\sigma_n}, \quad (18)$$

where $\sigma_n = \text{sgn}[\varphi''(z_n)]$.

Therefore, the transition amplitude and probability become

$$\mathcal{A}_{a \rightarrow n} \simeq \epsilon \sum_n \sqrt{\frac{2\pi\delta_{A'}^2(z_n)}{|\varphi''(z_n)|}} e^{i[\varphi(z_n) + \frac{\pi}{4}\sigma_n]}, \quad (19)$$

$$P_{a \rightarrow n} = |\mathcal{A}_{a \rightarrow n}|^2 = \epsilon^2 \left[\sum_n A_n + \sum_{n < m} 2\sqrt{A_n A_m} \cos(\varphi_{nm}) \right], \quad (20)$$

where the individual resonance contribution is defined as

$$A_n = \frac{2\pi\delta_{A'}^2(z_n)}{|\varphi''(z_n)|}, \quad (21)$$

and the accumulated phase between two resonances is

$$\varphi_{nm} = \varphi(z_n) - \varphi(z_m) + \frac{\pi}{4}(\sigma_n - \sigma_m) \simeq \int_{z_m}^{z_n} dz (\delta(z) - \delta_{A'}). \quad (22)$$

When the phase difference satisfies $\varphi_{nm} \gg 2\pi$ (corresponding to many oscillations within the observational bandwidth or line-of-sight variations), the interference term averages to zero, and the probability reduces to the incoherent sum [33, 34]

$$P_{a \rightarrow s} \simeq \epsilon^2 \sum_n A_n, \quad (23)$$

which corresponds to the non-adiabatic LZ limit, where single-resonance probabilities add incoherently and phase effects are neglected.

This stationary-phase treatment remains valid as long as the background potential varies monotonically near each resonance. In the next subsection, we discuss the breakdown of this approximation for non-monotonic potentials, where the resonant conversion occurs close to a local extremum of the in-medium photon mass and the standard LZ description no longer applies.

C. Breakdown of the Landau-Zener approximation for non-monotonic potential

When the DP mass lies near a local extremum of the in-medium photon mass, $m_\gamma(z)$, two nearby resonances z_1 and z_2 appear and approach one another as $m_{A'} \rightarrow m_\gamma(z_{\text{crit}})$. At

the critical mass

$$m_{A'} = m_\gamma(z_{\text{crit}}) \equiv m_{\text{crit}}, \quad (24)$$

the two resonances coalesce at the extremum z_{crit} . Near this point, the first two derivatives of the phase vanish,

$$\varphi'(z_{\text{crit}}) = \varphi''(z_{\text{crit}}) = 0, \quad \varphi'''(z_{\text{crit}}) \neq 0, \quad (25)$$

and the usual single-saddle LZ treatment fails. The departure from the LZ regime is characterized by

$$\xi = \frac{\varphi''(z_n)}{|\varphi'''(z_{\text{crit}})|^{2/3}}, \quad (26)$$

with $\xi \lesssim 1$ indicating the breakdown region.

Expanding around z_{crit} , the phase and diagonal terms become

$$\varphi(z) \simeq \varphi(z_{\text{crit}}) + \frac{1}{3!} \varphi'''(z_{\text{crit}}) (z - z_{\text{crit}})^3, \quad (27)$$

$$\delta_{A'}(z) \simeq \delta_{A'}(z_{\text{crit}}) + \delta'_{A'}(z_{\text{crit}}) (z - z_{\text{crit}}), \quad (28)$$

and introducing the Airy rescaling

$$u = \sigma_c \left(\frac{\varphi'''(z_{\text{crit}})}{2} \right)^{1/3} (z - z_{\text{crit}}), \quad dz = \left(\frac{2}{|\varphi'''|} \right)^{1/3} du. \quad (29)$$

Following Eq. 11, the transition probability becomes

$$P_{a \rightarrow n} \simeq \epsilon^2 \left| \left(\frac{2}{|\varphi'''|} \right)^{1/3} \int du \left[\delta_{A'}(z_{\text{crit}}) + \sigma_c \left(\frac{2}{|\varphi'''|} \right)^{1/3} u \delta'_{A'}(z_{\text{crit}}) \right] e^{i(\zeta u + \frac{u^3}{3})} \right|^2, \quad (30)$$

where $\zeta = \sigma_c (2/|\varphi'''|)^{1/3} \varphi'$. Using the standard Airy integrals

$$2\pi Ai(\zeta) = \int_{-\infty}^{\infty} du e^{i(u^3/3 + \zeta u)}, \quad 2\pi Ai'(\zeta) = \int_{-\infty}^{\infty} du u e^{i(u^3/3 + \zeta u)}, \quad (31)$$

the compact result for the conversion probability is obtained as [35]

$$P_{a \leftrightarrow n} \simeq 4\pi^2 \epsilon^2 \delta_{A'}^2 \left(\frac{2}{|\varphi'''|} \right)^{2/3} \left[Ai(-\zeta) + i\sigma_c \left(\frac{2}{|\varphi'''|} \right)^{1/3} \left(\frac{\delta'_{A'}}{\delta_{A'}} - \frac{\varphi''''}{6\varphi'''} \right) Ai'(-\zeta) \right]_{z=z_{\text{crit}}}^2. \quad (32)$$

Equation 32 applies in the vicinity of the critical point, ($m_{A'} \simeq m_{\text{crit}}$), where $\xi \lesssim 1$ and the standard LZ approximation no longer holds.

III. PHOTON-DARK PHOTON OSCILLATION IN MESSIER 87 SUPERMASSIVE BLACK HOLE BACKGROUND

In this section, we explore three representative electron-density models adopted for the environment around the M87 BH and describe their corresponding plasma profiles. Using these density models, we analyze the variation in the probability of photon-DP conversion with the oscillation length scale and the deviation of the DP mass from its critical value. The behavior of the oscillation probability is explored for different choices of the electron density profile and critical mass parameter, considering both monotonic and non-monotonic plasma potentials.

A. Electron Density Profiles Around M87*

The plasma surrounding the SMBH M87* is often modeled using simplified accretion prescriptions. A standard choice is the spherical (Bondi-like) accretion model, which assumes a steady, spherically symmetric inflow. Imposing a constant mass accretion rate,

$$\dot{M} = 4\pi r^2 \rho v_r, \quad (33)$$

and adopting a free-fall velocity profile $v_r \propto r^{-1/2}$, the density scales as $\rho \propto r^{-3/2}$. The corresponding electron number density follows a monotonic power-law profile [71–76]

$$n_e(r) = n_0 \left(\frac{r}{r_{\text{ph}}} \right)^{-3/2}, \quad (34)$$

where n_0 denotes the electron density near the photon sphere with radius r_{ph} . For M87*, the photon sphere radius is approximately $r_{\text{ph}} \simeq 6.2 \times 10^{-7}$ kpc from the center of the SMBH.

The radiative accretion flow models [73] predict that the plasma in the vicinity of the event horizon is hot and magnetized, with electron temperatures $T_e \sim 10^9$ K and magnetic fields of order (1–30) G. For M87, mm-wavelength observations imply electron densities $n_e \sim 10^5$ – 10^7 cm $^{-3}$ at radii $r \simeq (5\text{--}10) r_g$ (where $r_g = GM$ is the gravitational radius), are consistent with sub-Eddington accretion rates of $\dot{M} \sim 10^{-5} M_{\odot}$ yr $^{-1}$. These values correspond to a dilute, optically thin, magnetically dominated plasma environment. Since, the magnetic field is relatively weak, QED-induced photon mass corrections are negligible,

and the effective photon mass is instead governed by the plasma frequency,

$$m_{\text{eff}}(r) \simeq \omega_{\text{pl}}(r) = \sqrt{\frac{4\pi\alpha n_e(r)}{m_e}}, \quad (35)$$

so that resonant photon-DP mixing is dictated by the interplay between the plasma mass and the DP mass. Here, in Eq. 35, α denotes the fine structure constant and m_e denotes the electron mass. For our analysis, we adopt a reference electron number density $n_0 = 10^6 \text{ cm}^{-3}$, motivated by accretion based modeling studies of the environment surrounding M87*, as discussed above.

We also consider a spherically symmetric plasma distribution motivated by accretion-disk simulations, which can be approximated by a log-normal profile [77]

$$n_e(r) = n_{\text{max}} \exp \left[-\frac{(\ln(r/r_m))^2}{2\sigma^2} \right], \quad (36)$$

where r_m denotes the radius at which the density peaks, σ determines the width of the distribution, and n_{max} is the maximum density. For illustration, we adopt $r_m = 3r_{\text{ph}}$ and $n_{\text{max}} \sim 10^8 \text{ cm}^{-3}$, consistent with plasma densities required to generate radio emission at MHz frequencies in the inner flow. A representative value $\sigma = 0.5$ yields a moderately narrow peak, producing two spatial locations along the line of sight where $m_{A'} = m_{\text{eff}}(r)$. These dual resonances naturally give rise to coherent interference between successive level crossings, enhancing the overall photon-DP conversion probability. This behavior is well described by the multiple level crossing formalism developed for non-monotonic plasma potentials as described in Section II.

To complement these near-horizon models, we additionally adopt free-electron density profiles from [78], based on the Illustris-TNG300 cosmological magnetohydrodynamical simulations [79–81]. The Illustris and its successor Illustris TNG projects aim to model the universe from shortly after the big bang to the present epoch, capturing the coupled dynamics of DM, baryons, and the SMBHs within the standard cosmological framework. TNG300 with a box size of 300 Mpc provides an unparalleled statistical environment for studying massive galaxies and clusters, including M87-like systems. In Virgo-like cluster analogous with total masses $(6.3 \pm 0.9) \times 10^{14} \text{ M}_\odot$, the number density reaches 10^{-2} cm^{-3} within the inner tens of kpc and remains at 10^{-3} cm^{-3} on scales of several hundred kpc. Such an extended and coherent field structure may also provide a suitable environment for photon-DP

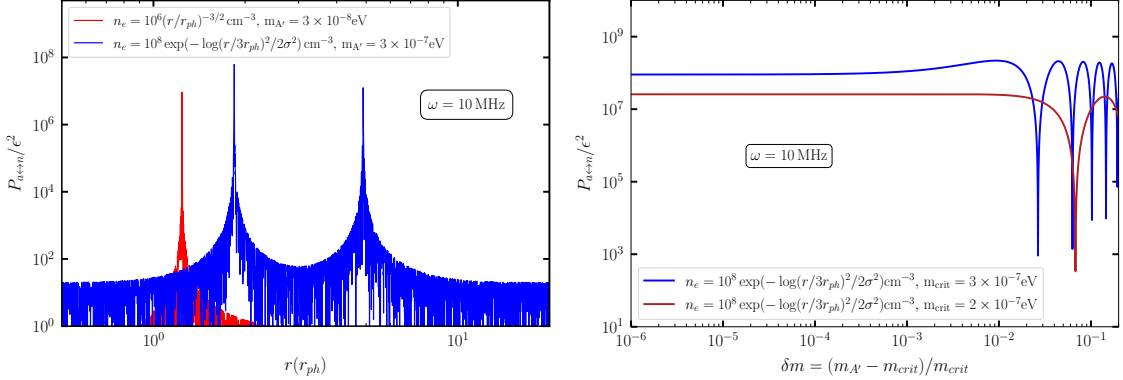


FIG. 1. Conversion probability $P_{a\leftrightarrow n}/\epsilon^2$ for photon-DP mixing. *Left Panel:* Probability as a function of distance for a monotonic power-law plasma profile (red) showing a single resonance near the photon-sphere radius, and for a non-monotonic log-normal profile (blue) exhibiting two resonant locations. *Right Panel:* Probability plotted against the mass-deviation parameter δm , computed using the multiple-level-crossing approximation Eq. 32 and evaluated at the plasma peak $r_m = z_c$.

conversion. This plasma profile as presented in [78], decreases with distance and is treated as monotonic profile in the present study.

B. Photon-dark photon conversion probabilities in different plasma profiles around M87*

In this section, we present the conversion probability between DPs and ordinary photons. Using the power-law plasma profile Eq. 34, which enters in $\delta(z)$, the transition probability $P_{a\leftrightarrow n}$ is obtained from the standard expression Eq. 15. For a monotonic plasma profile, the probability attains its maximum value at the distance L for which $\delta(z) = \delta_{A'}$. In left panel of FIG. 1 we show the probability, $P_{a\leftrightarrow n}/\epsilon^2$, as a function of distance (red curve), evaluated for a DP mass $m_{A'} = 3 \times 10^{-8} \text{ eV}$ and a photon frequency of 10 MHz. A sharp resonance appears near the photon-sphere radius ($r/r_{ph} = 1.5$) when the central number density is $n_0 = 10^6 \text{ cm}^{-3}$.

For comparison, we also show the probability obtained for a non-monotonic, log-normal plasma profile Eq. 36 (blue curve). As illustrated in left panel of FIG. 1, this profile yields two distinct resonant locations, reflecting the non-monotonic behavior of the plasma distribution.

The plot corresponds to $m_{A'} = 3 \times 10^{-7}$ eV and $n_0 = 10^8$ cm $^{-3}$, with the width parameter of the log-normal distribution fixed at $\sigma = 0.5$, which produces a moderately peaked profile.

In the right panel of FIG. 1, we show $P_{a \leftrightarrow n}/\epsilon^2$ as a function of the DP mass deviation relative to the critical mass m_{crit} , i.e., $\delta m = (m_{A'} - m_{\text{crit}})/m_{\text{crit}}$. This plot is obtained using the approximate expression applicable to systems with multiple level crossings Eq. 32, at fixed m_{crit} with the values 2×10^{-7} eV (red curve) and 3×10^{-7} eV (blue curve) and photon frequency ω . These benchmark values of the critical mass are selected to maximize the conversion probability for the given plasma density, frequencies around 10 MHz, and an oscillation length of the order of r_{ph} . For the same non-monotonic plasma profile adopted in left figure of FIG. 1, we compute the required derivatives ϕ''' and ϕ'''' and evaluate the transition probability at $z = z_c$, the location of the plasma peak. This resonant distance z_c corresponds to the value of m_{crit} for which the plasma number density is maximized.

We do not show the DP-photon conversion probability computed using the Illustris-TNG plasma density profile for the SMBH environment in FIG. 1 for the following reason. The plasma distribution extracted from the Illustris-TNG simulation characterizes the large-scale galactic medium, with typical length scales extending to kpc and beyond, whereas FIG. 1 corresponds to plasma profiles on much smaller, near-horizon scales. While the conversion probability is not displayed, the corresponding constraints on the coupling are derived using the Illustris-TNG plasma profile and presented in Section. VI.

IV. PHOTON-DARK PHOTON OSCILLATION IN CRAB NEBULA BACKGROUND

In this section, we examine the non-monotonic behavior of the effective mass relevant for photons associated with the Crab Nebula emission. The Crab Nebula is a pulsar wind Nebula powered by the central Crab pulsar. The relativistic wind of the pulsar injects particles and energy into the Nebula and drives its observed radiation [67, 82]. The photons considered here originate near the pulsar and initially propagate through its magnetospheric plasma and we therefore employ the standard Goldreich-Julian(GJ) model [83] for this NS magnetosphere, in which the GJ charge density determines the plasma-induced photon mass. We also analyze the resulting photon-DP conversion probability in the GJ background of Crab Nebula.

A. Electron density profiles in Crab Nebula background

The plasma environment in the Crab pulsar magnetosphere varies strongly with both radial and angular distances, leading to substantial changes in the plasma-induced photon mass as photons propagate through the magnetosphere. Rotation of the NS generates an induced electric field that exceeds the gravitational binding energy at the stellar surface. As a result, surface charges are stripped off and flow along magnetic field lines until they redistribute such that the local Lorentz force vanishes. This establishes a corotating magnetosphere whose electron number density is well described by the GJ prescription as

$$n_e^{\text{GJ}}(r, \theta) = \frac{2\Omega \cdot \mathbf{B}}{e} \left[\mathcal{F}_1(r_{\text{red}}) \sin^2 \theta - \mathcal{F}_2(r_{\text{red}}) (\sin^2 \theta - 2 \cos^2 \theta) \right], \quad (37)$$

where the functions in the square brackets encode the relativistic corrections to the canonical GJ density, given as

$$\begin{aligned} \mathcal{F}_1(r_{\text{red}}) = r_{\text{red}}^3 & \left\{ \left(1 - \frac{\kappa}{r_{\text{red}}^3} \right) \left[\frac{2}{r_{\text{red}} - 1} - \frac{1}{(r_{\text{red}} - 1)^2} + 2 \ln \left(1 - \frac{1}{r_{\text{red}}} \right) \right] \right\} + \\ & \left(2 + \frac{\kappa}{r_{\text{red}}^3} \right) \left\{ \frac{1}{r_{\text{red}}} + \frac{1}{r_{\text{red}} - 1} + 2 \ln \left(1 - \frac{1}{r_{\text{red}}} \right) \right\}, \end{aligned} \quad (38)$$

and

$$\mathcal{F}_2(r_{\text{red}}) = r_{\text{red}}^3 \frac{2 \left(1 - \frac{\kappa}{r_{\text{red}}^3} \right)}{1 - \frac{1}{r_{\text{red}}}} \left\{ \frac{1}{2r_{\text{red}}^2} + \frac{1}{r_{\text{red}}} + \ln \left(1 - \frac{1}{r_{\text{red}}} \right) \right\}, \quad (39)$$

where $r_{\text{red}} = r/r_g$ and $\kappa = 2/5(R/r_g)^2$ with R denotes the radius of the NS, Ω denotes its angular velocity, B is the magnetic field and e stands for the electric charge. Considering the magnetic field is dipolar outside the star and the magnetic moment axis is tilted by an angle α_m with the rotation axis, which is necessary for the pulsed radiation, and also consider that the angular velocity is along the z axis, Eq. 37 becomes

$$n_e^{\text{GJ}}(r, \theta) = \frac{B_0}{eR_{\text{LC}}} \left(\frac{R}{r} \right)^3 (3 \cos \theta \hat{\mathbf{m}} \cdot \hat{\mathbf{r}} - \cos \alpha_m) \left[\mathcal{F}_1(r_{\text{red}}) \sin^2 \theta - \mathcal{F}_2(r_{\text{red}}) (\sin^2 \theta - 2 \cos^2 \theta) \right], \quad (40)$$

where B_0 denotes the surface magnetic field of the magnetized star, $R_{\text{LC}} = 1/\Omega$ denotes the light cylinder (LC) radius, $\hat{\mathbf{m}}$ denotes the direction of the magnetic moment axis and

$$\hat{\mathbf{m}} \cdot \hat{\mathbf{r}} = \cos \theta \cos \alpha_m + \sin \theta \sin \alpha_m \cos(\Omega t). \quad (41)$$

The LC radius marks the distance out to which plasma in the magnetosphere can corotate with the NS. Since the corotating charges have tangential velocity $\mathbf{v} = \Omega \times \mathbf{r}$, their speed

increases linearly with radius. For a fixed angular velocity Ω , causality requires that this velocity never exceed the speed of light. The point at which $v = 1$ (speed of light in vacuum) defines the LC radius, yielding $R_{\text{LC}} = 1/\Omega$. In regions where the magnetic field strength satisfies $B(r) \gtrsim B_c = m_e^2/e$, both the magnetic field and the plasma contribute to the effective photon mass, but with opposite signs. The total effective mass may be written as

$$m_\gamma^2 = V_{\text{QED}} + V_{\text{pl}}, \quad (42)$$

where the quantum electrodynamics (QED) contribution is

$$V_{\text{QED}} \simeq -\frac{7\alpha}{45\pi} b_{\text{red}}^2 \eta \omega^2 \sin^2 \theta, \quad (43)$$

with $b_{\text{red}} = B(r)/B_c$, where the radial component of the magnetic field, $B(r)$, falls off as $1/r^3$ outside the NS. The function η encodes the leading behavior in both the weak-and strong-field limits and is well approximated by

$$\eta = \frac{1 + 1.2b_{\text{red}}}{1 + 1.33b_{\text{red}} + 0.56b_{\text{red}}^2}. \quad (44)$$

The term V_{QED} arises from standard quantum electrodynamical effects such as vacuum birefringence, photon splitting, and magnetic pair production. The plasma contribution, sourced by the GJ charge density, takes the form

$$V_{\text{pl}} = \omega_{\text{pl}}^2 \sin^2 \theta, \quad (45)$$

where $\omega_{\text{pl}}^2 = 4\pi\alpha n_e^{\text{GJ}}/m_e$ is the plasma frequency with α the fine structure constant and m_e denotes the mass of the electron. Because V_{QED} and V_{pl} carry opposite signs, their competition naturally produces a non-monotonic radial dependence of the effective photon mass, independent of the specific relativistic correction functions.

The radial behavior of the two potential terms differs significantly. The plasma contribution scales as $1/r^3$, whereas the QED term falls off more rapidly as $1/r^6$. At intermediate radii, where V_{QED} dominates, the effective photon mass becomes negative, $m_\gamma^2 < 0$, owing to the negative sign of the QED potential. Conversely, at larger radii the plasma term prevails and $m_\gamma^2 > 0$. Because the two contributions have opposite signs, there is a turnover point denoted the critical radius at which

$$V_{\text{pl}}(r_{\text{crit}}) \simeq -V_{\text{QED}}(r_{\text{crit}}). \quad (46)$$

This condition yields

$$r_{\text{crit}} \sim (\omega^2 R_{\text{LC}} B_0)^{1/3} \frac{eR}{m_e}, \quad (47)$$

and defines an associated critical mass,

$$m_{\text{crit}} \sim \frac{m_e}{e\omega R_{\text{LC}}}. \quad (48)$$

The non-monotonic nature of $m_\gamma^2(r)$ implies that when the DP mass lies near m_{crit} , two resonance points appear in close proximity, one near the stellar surface R and the other near the LC radius R_{LC} . Requiring the critical radius to fall within the interval $R \lesssim r_{\text{crit}} \lesssim R_{\text{LC}}$ leads to the condition

$$\frac{1}{R_{\text{LC}}} \lesssim \frac{\omega^2 B_0 e^2}{B_c m_e} \lesssim \frac{R_{\text{LC}}^2}{R^3}. \quad (49)$$

B. Photon-dark photon conversion probabilities in the plasma of Crab Nebula

In FIG. 2 we present the photon-DP conversion probability $P_{a \leftrightarrow n}$ as a function of the deviation parameter δm in the magnetospheric environment of the Crab pulsar. The curves are obtained by fixing the critical mass to $m_{\text{crit}} = 10^{-7}$ eV, the photon energy to 4×10^{-5} eV, and by considering two oscillation lengths, $r_0 = 250$ km and $r_0 = 500$ km. For the Crab pulsar, we adopt the LC radius $R_{\text{LC}} = T/2\pi \sim 1600$ km, with rotation period $T = 33$ ms, and a magnetic-field strength satisfying $B_0/B_c = 0.2$, characteristic of this source.

The red curve corresponds to $r_0 = 250$ km, while the blue curve shows the result for $r_0 = 500$ km. As shown, the peak conversion probability increases with the oscillation distance. At larger values of δm , the highly oscillatory behavior reflects the non-monotonic structure of the pulsar magnetospheric potential entering through $\delta(z)$. In the regime $\delta m \ll 1$, the probability approaches a constant value, and the approximate expression Eq. 32 is required to accurately capture the behavior near the multiple-level-crossing resonance.

V. SPECTRAL MODELING AND DATA ANALYSIS

In this section, we model the observed spectra of M87 and the Crab Nebula using LOFAR measurements and broadband SED data, respectively. In both cases, the intrinsic emission is well described by a power-law spectrum. For illustrative purposes, we introduce photon-DP mixing with a representative choice of oscillation parameters and fit the resulting modified

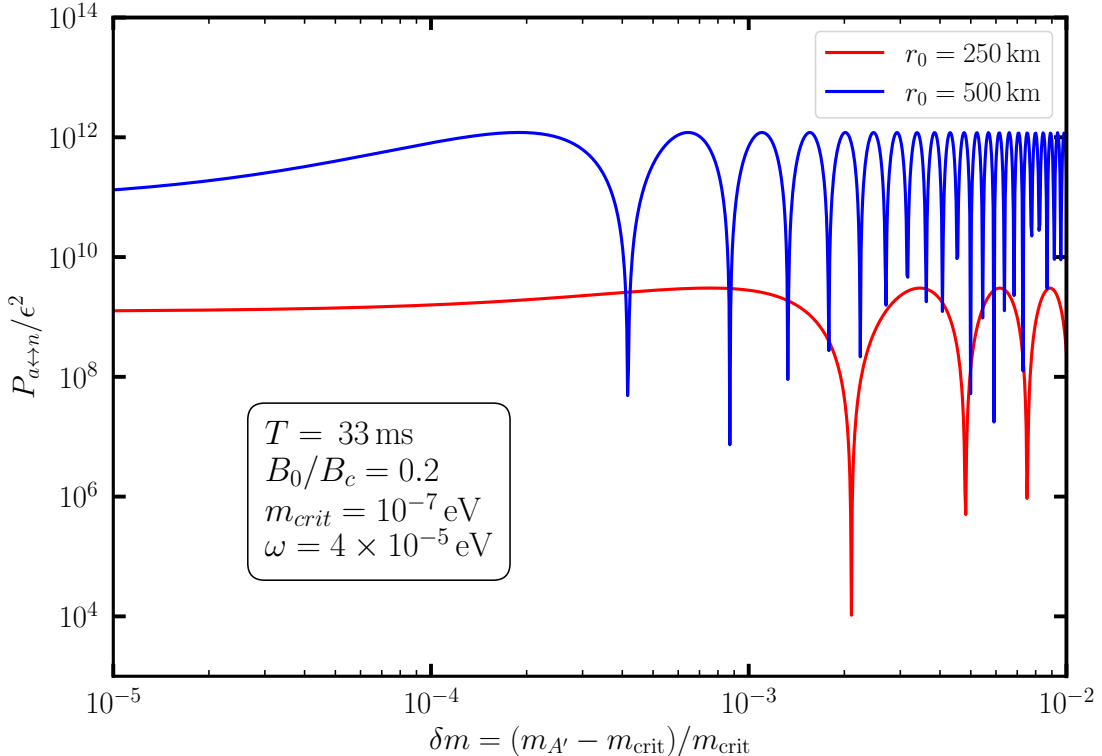


FIG. 2. DP-photon conversion probability $P_{a\leftrightarrow n}$ as a function of the deviation parameter δm in the Crab pulsar magnetosphere. The curves correspond to oscillation distances of $r_0 = 250$ km (red) and $r_0 = 500$ km (blue), computed for $m_{\text{crit}} = 10^{-7}$ eV and a photon energy of 4×10^{-5} eV. The pronounced oscillatory structure originates from the non-monotonic magnetospheric potential, whereas in the $\delta m \ll 1$ regime, the probability approaches a constant value, reflecting the need for the approximate expression Eq. 32 in the multiple-level crossing scenario.

spectrum to the observational data while retaining the same underlying power law form. The procedure is outlined below.

A. LOFAR data and M87*:

We make use of low-frequency radio observations of the M87 galaxy obtained with the LOFAR array, covering the 10 – 1000 MHz band, as indicated by the blue color bar in the left panel of FIG. 3. The central radio source associated with M87 is commonly identified as Virgo A, for which there is an extensive archival data and numerous literatures have modeled it [58–64, 84, 85].

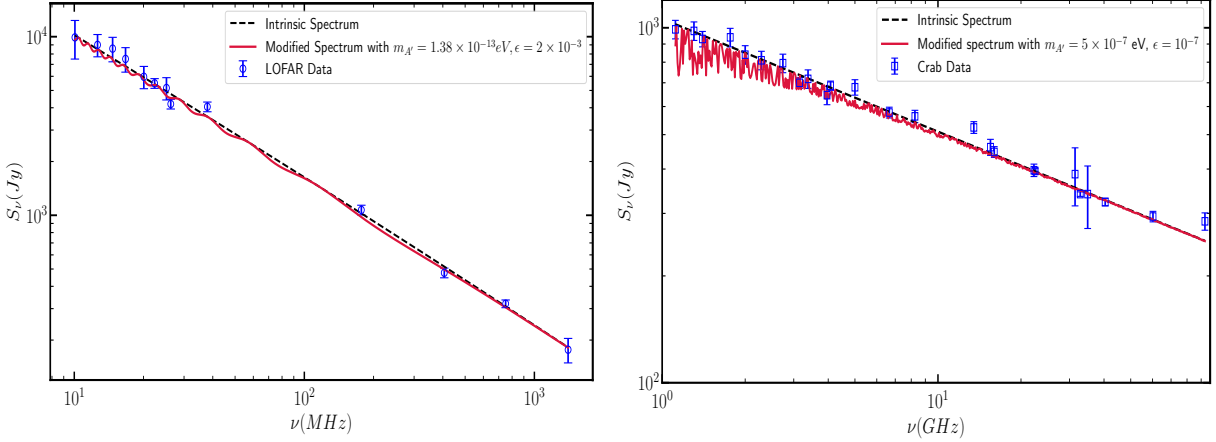


FIG. 3. *Left panel:* Intrinsic and DP-modified radio spectrum of the M87* SMBH environment, using LOFAR data. The solid curve shows the distorted spectrum for the benchmark parameters $m_{A'} = 1.38 \times 10^{-13}$ eV and $\epsilon = 2 \times 10^{-3}$. *Right Panel:* Intrinsic and DP-modified spectrum of the Crab Nebula. The red curve corresponds to the benchmark point $m_{A'} = 5 \times 10^{-7}$ eV and $\epsilon = 10^{-7}$. Both panels illustrate how DP-photon conversion alters the radio continuum relative to the intrinsic emission models.

For our analysis, we adopt the intrinsic flux-density model introduced in [85], which provides an excellent fit to the LOFAR data when expressed in logarithmic frequency space. The intrinsic spectrum is parametrized as

$$S_{\text{in}}(\nu) = A_0 \times 10^{A_1 \log_{10}(\frac{\nu}{150 \text{ MHz}}) + A_2 [\log_{10}(\frac{\nu}{150 \text{ MHz}})]^2} \text{ Jy}, \quad (50)$$

where ν denotes the observing frequency. The best-fit parameters are $A_0 = 1.17 \times 10^3$ Jy, where Jy stands for “Jansky”, used as the unit of flux, $A_1 = -0.81$, and $A_2 = -0.01$ yield an accurate representation of the intrinsic radio emission arising from the plasma near the central SMBH of M87 which is shown in black dashed curve in the left panel of FIG. 3.

In addition to the intrinsic spectrum, we also show the modified flux predicted in the presence of photon-DP conversion. The modification arises from the frequency-dependent survival probability of photons propagating through the plasma environment surrounding the SMBH, which induces a characteristic distortion of the radio continuum. The resulting spectrum, shown as a solid red curve in the left panel of FIG. 3, corresponds to a benchmark choice of DP parameters $m_{A'} = 1.38 \times 10^{-13}$ eV and $\epsilon = 2 \times 10^{-3}$. This illustrates how the expected deviation from the intrinsic spectrum varies across the LOFAR band and highlights

the frequencies at which the conversion effect produces the strongest suppression.

B. SED data and Crab Nebula:

The Crab Nebula has been extensively observed across a broad frequency range, from radio to sub-millimeter wavelengths [86–88]. A comprehensive spectral energy distribution is analyzed in [86], where the emission below ~ 100 GHz is dominated by a single synchrotron component produced by relativistic electrons in the pulsar wind Nebula. No significant thermal or dust contribution is required in this regime, and the observed fluxes are well described by a power-law spectrum of the form $A\nu^\beta$.

For frequencies up to ~ 100 GHz, the best-fit spectral index is $\beta \simeq -0.3$, with no indication of a low-frequency turnover or additional curvature. This implies that processes such as free-free absorption or synchrotron aging contribute only marginally in the radio band, making this frequency range a reliable baseline for probing possible deviations from the intrinsic synchrotron emission, including photon-DP mixing effects.

Accordingly, in our analysis we model the intrinsic Crab Nebula spectrum with the power law fit to the low frequency data,

$$S_{\text{in}}(\nu) = 970 \left(\frac{\nu}{1 \text{ GHz}} \right)^{-0.31} \text{ Jy}, \quad (51)$$

where the normalization and spectral index are obtained from the best fit to the observed radio fluxes.

The intrinsic power-law spectrum is indicated by the black dashed line in the right panel of FIG. 3. In addition to this, we also compute the modified flux expected in the presence of photon-DP conversion within the Crab pulsar magnetosphere. Because the effective mixing potential becomes non-monotonic due to the competing plasma and QED contributions, the resulting photon survival probability exhibits multiple level crossings and a characteristic frequency dependence. This induces a distortion in the observed radio spectrum whose magnitude and shape depend on the DP parameters and the assumed oscillation distance.

In right panel of FIG. 3 we show, in red, the modified spectrum corresponding to the benchmark choice $m_{A'} = 5 \times 10^{-7}$ eV and $\epsilon = 10^{-7}$. The deviation from the intrinsic synchrotron spectrum becomes most pronounced in the frequency bands where the conversion probability is enhanced by resonant or near-resonant mixing. This comparison illustrates

how photon-DP oscillations may imprint detectable spectral signatures in the well-measured low-frequency emission of the Crab Nebula.

VI. LIMITS ON PHOTON-DARK PHOTON KINETIC MIXING

If DPs exist and are produced via photon-DP conversion in the plasma, they would imprint characteristic distortions on the observed spectrum. The resulting flux can be expressed as

$$S_{\text{th}}(m_{A'}, \epsilon) = S_{\text{in}}[1 - P_{a \leftrightarrow n}(m_{A'}, \epsilon)]. \quad (52)$$

For the SMBH scenario, the intrinsic spectrum S_{in} follows Eq. 50, while for the Crab emission, it is given in Eq. 51.

To constrain these parameters, we compare the theoretical spectrum with the data using a chi-squared statistics,

$$\chi^2(m_{A'}, \epsilon) = \sum_{i=1}^N \left[\frac{S_{\text{obs}}^i - S_{\text{th}}^i(m_{A'}, \epsilon)}{\sigma_{\text{obs}}^i} \right]^2, \quad (53)$$

In this expression, S_{obs}^i and σ_{obs}^i represent the observed flux and its corresponding uncertainty in the i -th frequency bin, whereas S_{th}^i is evaluated using Eq. 52.

While the least-squares framework allows for parameter estimation at arbitrary confidence level (C.L.), in this work we adopt the 95% C.L., corresponding to $\Delta\chi^2 = 6.18$ for two degrees of freedom.

A. Constraints from Spectral Modeling of the M87* Environment

With the intrinsic spectrum Eq. 50 of the emission near the SMBH M87* (see Section. V), we compare the expected spectral distortion induced by DP to photon conversion with the observed LOFAR data. This allows us to place constraints on the kinetic mixing parameter ϵ for fixed DP masses.

For the SMBH environment, we consider several plasma-density profiles. In the case of a monotonic power-law profile, the DP-photon conversion probability is evaluated for two distinct oscillation-length scales: (i) a region very close to the photon sphere, $r_0 = 5 r_{\text{ph}}$, and (ii) a much larger radius of order $\mathcal{O}(1 \text{kpc})$. The corresponding constraints are shown in FIG. 4 as dashed and dot-dashed purple curves, with the LOFAR 95% excluded region

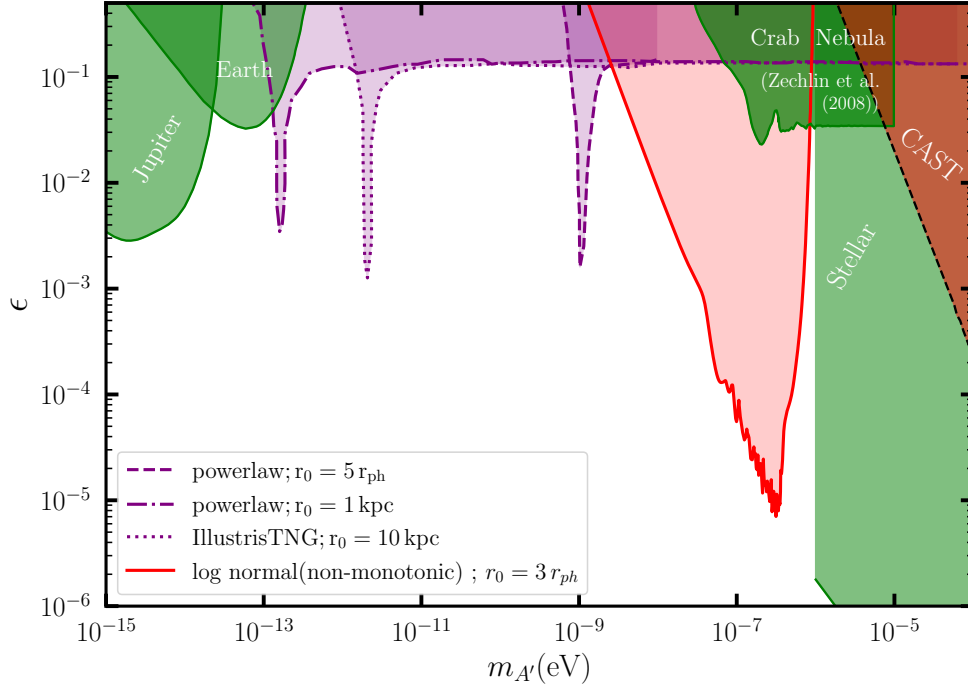


FIG. 4. Constraints on the kinetic mixing parameter ϵ as a function of the DP mass $m_{A'}$. The purple dashed and dot-dashed curves correspond to the cases where the DP-photon oscillation occurs near the photon sphere ($r_0 = 5 r_{\text{ph}}$) and at 1 kpc scales, respectively, assuming a monotonic plasma profile. The dotted purple curve shows the limits obtained using the large-scale plasma density from the TNG300 simulation. The filled purple region indicates the parameter space excluded at the 95% C.L. from the LOFAR radio observations. The red solid curve represents the constraint for a non-monotonic plasma profile near the SMBH, where multiple level crossings enhance the conversion probability. For comparison, other astrophysical and laboratory bounds are shown which are taken from the `AxionLimits` database [37].

is represented by the filled band. We additionally incorporate a large-scale plasma-density estimate obtained from the TNG300 simulations, whose resulting limits are plotted as the dotted purple curve.

As the figure illustrates, increasing the oscillation distance generally strengthens the bounds at lower DP masses. Conversely, for oscillation regions restricted to a few photon-sphere radii, the constraints tighten toward higher DP masses. The sharp dips in the exclusion curves originates from the oscillatory phase of the DP-photon conversion probability.

At specific values of the DP mass, the phase-matching condition, $(\delta(z) - \delta_{A'})r_0 \sim \mathcal{O}(1)$ leads to constructive interference over the fixed propagation distance, maximizing the conversion probability. Consequently, a smaller mixing ϵ is sufficient to produce the same signal, resulting in a localized deep feature in the bound.

Across the monotonic plasma profile scenarios, the strongest constraints reach at $\epsilon \sim 10^{-3}$. For oscillation distances of $r_0 = 5 r_{\text{ph}}$ and $r_0 = 1 \text{ kpc}$ corresponding to the power law plasma profiles, and $r_0 = 10 \text{ kpc}$ for the IllustrisTNG profile, the most stringent constraints are obtained at DP masses of $1.03 \times 10^{-9} \text{ eV}$, $1.13 \times 10^{-13} \text{ eV}$, and $2.07 \times 10^{-12} \text{ eV}$, respectively.

We also investigate a non-monotonic plasma profile in Section. III, for which the resulting constraint is shown as the solid red curve. The presence of multiple density turning points near the SMBH induces multiple level crossings, enhancing the overall DP-photon conversion probability. Consequently, the resulting limits are significantly stronger than those from monotonic profiles. For this case, the most stringent bound occurs at a DP mass of $m_{A'} = 5 \times 10^{-7} \text{ eV}$, yielding a kinetic mixing constraint of $\epsilon \simeq 7 \times 10^{-6}$.

For completeness, we compare our constraints with existing astrophysical bounds obtained from Jupiter [49], Earth-based atmospheric observations [48], and nebular environments ¹, where similar conversion processes may occur. We additionally display the combined stellar-evolution limits and those from CAST [42]. Laboratory bounds are not included in the figure, as our focus here is on astrophysical constraints in the relevant mass window.

While laboratory experiments provide strong bounds in this mass range, our analysis offers competitive constraints from astrophysical environments, thereby extending the sensitivity of indirect searches beyond terrestrial setups. In particular, within this mass regime our results represent competitive to the available astrophysical constraints, highlighting the complementary role of galaxy- and SMBH-based probes. Moreover, the limits derived here are largely independent of the assumption that DP constitute the entirety of the DM, relying instead on conversion processes governed by environmental plasma properties.

¹ The bound reported by Zechlin et al. [89] is obtained from very-high-energy ($\mathcal{O}(\text{TeV})$) gamma-ray observations of the Crab Nebula with Cherenkov telescopes. In that analysis, the propagation effects associated with the ambient plasma profile were not considered.

B. Constraints from Spectral Modeling of Crab Nebula

In the case of the Crab spectrum, we perform an analogous analysis to derive exclusion limits in the ϵ - $m_{A'}$ parameter space. Owing to the fact that the plasma contribution and the QED vacuum polarization term enter the effective potential with opposite signs, the resulting profile becomes non-monotonic. Consequently, the conversion probability of DPs into photons must be evaluated using the formalism appropriate for multiple level crossings. The resulting 95% exclusion limits are displayed as solid blue curves in both panel of FIG. 5.

For the Crab pulsar, we assume a surface magnetic field strength $B_0 = 0.2 B_c$, where B_c is the critical magnetic field. The rotation period is taken to be $T = 33$ ms, implying a LC radius $R_{\text{LC}} = T/(2\pi)$. We consider two representative choices of the oscillation distance. For an oscillation length of 200 km, the corresponding limits appear in left panel of FIG. 5, while the bounds obtained for an oscillation length of 1000 km are shown in the right panel of FIG. 5.

We additionally display projected sensitivities for enhanced magnetic field strengths, with $B_0 = 10 B_c$ and $B_0 = 1000 B_c$, indicated by dashed and dot-dashed blue curves, respectively. The strongest constraint for the Crab pulsar in the 200 km scenario occurs at $\epsilon = 6 \times 10^{-6}$ for a DP mass $m_{A'} \simeq 1.3 \times 10^{-7}$ eV. In the 1000 km case, the tightest bound is $\epsilon \simeq 8 \times 10^{-7}$ at $m_{A'} \simeq 4 \times 10^{-9}$ eV. These sharp features arise in regions where the QED correction competes with the plasma contribution of the pulsar magnetosphere, leading to maximal conversion.

The strongest sensitivities in the $m_{A'}\text{-}\epsilon$ plane are obtained for $B_0/B_c = 10$ and $B_0/B_c = 1000$. For an oscillation distance of 200 km, the optimal sensitivities occur at $(m_{A'}, \epsilon) = (8.70 \times 10^{-7}$ eV, 8.08×10^{-7}) and $(8.32 \times 10^{-6}$ eV, 8.3×10^{-6}), respectively, as indicated through the dashed and dot-dashed curves in the left panel of FIG. 5. As evident from the figure, the projected sensitivity is competitive with existing stellar bounds in this mass range.

For a larger oscillation distance of 1000 km, the strongest projected sensitivities shift to $(2.53 \times 10^{-8}$ eV, 1.54×10^{-7}) for $B_0/B_c = 10$ and $(2.66 \times 10^{-7}$ eV, 1.57×10^{-8}) for $B_0/B_c = 1000$, as shown in the dashed and dot-dashed curves in the right panel of FIG. 5.

For comparison, we also show existing astrophysical constraints from stellar cooling [51, 90–92], very high energy gamma-ray observations from Crab Nebula [89] and CAST [42],

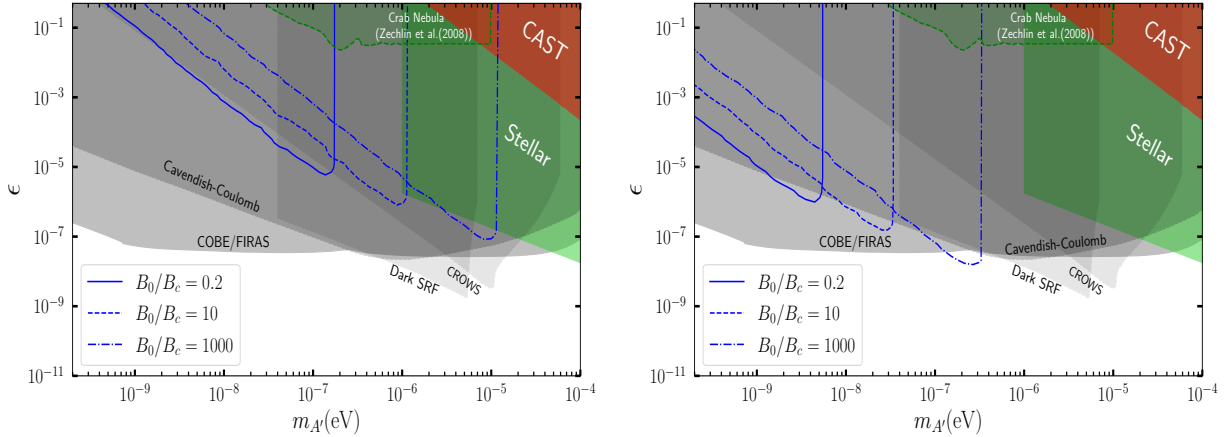


FIG. 5. Constraints on the kinetic mixing parameter ϵ from the Crab pulsar: *Left panel*: The 95% exclusion limits for an oscillation distance of $z = 200$ km. *Right panel*: The 95% exclusion limits for an oscillation distance of $z = 1000$ km. The solid blue curves represent the bounds obtained using the non-monotonic effective potential generated by the combined plasma and QED contributions in the Crab magnetosphere. Dashed and dot-dashed curves denote projected sensitivities for enhanced magnetic field strengths $B_0 = 10 B_c$ and $B_0 = 1000 B_c$, respectively. Existing astrophysical limits from stellar cooling and CAST, very high energy gamma-ray observations from Crab Nebula, together with laboratory constraints as well as cosmological bounds from COBE/FIRAS, are included for comparison and are taken from the `AxionLimits` database [37].

together with laboratory bounds (Dark SRF [93], Cavendish-Coulomb [39], CROWS [94]), including those from cosmological COBE/FIRAS bounds [53, 55], which are indicated in gray. Notably, projected sensitivities for stronger magnetic fields while keeping the pulsar radius and rotation period fixed can approach, and in some regimes surpass, the current laboratory bounds, particularly when the oscillation distance is large. For $B_0/B_c = 1000$, the projected limits approach and can challenge the strongest existing laboratory bounds. Overall, the strongest constraints arise at higher DP masses when the oscillation distance is short, whereas for lighter masses the limits tighten as the oscillation distance increases.

VII. CONCLUSIONS AND DISCUSSIONS

Compact astrophysical systems such as NS and BHs constitute highly sensitive and complementary laboratories for probing feebly coupled dark-sector physics. Focusing on ul-

tralight DPs that are kinetically mixed with the visible photon but do not comprise the DM, we study resonant photon-DP oscillations in monotonic and non-monotonic plasma environments relevant to M87* and the Crab pulsar-wind Nebula. In media with a monotonic plasma mass profile, photon-DP conversion is well described by a single avoided level crossing, and the standard LZ approximation reliably captures the transition probability using only local information at the resonance. In contrast, non-monotonic plasma profiles generically lead to multiple level crossings, for which the conversion probability cannot be obtained by treating each crossing independently. In this case, coherent interference between amplitudes generated at different crossings plays a crucial role, and the resulting phase depends on the integrated eigenvalue splitting between the crossings rather than solely on local properties at the resonance. Consequently, accurate predictions in realistic astrophysical environments require a global treatment of the propagation through non-monotonic media, beyond the standard single-crossing LZ framework.

We show that physically motivated non-monotonic plasma density profiles, including log-normal profiles applicable to the M87 environment and GJ charge densities with potential QED effects in the Crab Nebula, can lead to a substantial enhancement of resonant photon-DP conversion. This enhancement translates into constraints on the kinetic-mixing parameter that are several orders of magnitude stronger than those derived assuming monotonic plasma density profiles. This enhancement arises because non-monotonic plasma profiles around M87 and Crab Nebula admit multiple resonant crossings with reduced local density gradients, increasing the adiabaticity of the transition and allowing coherent interference between successive LZ crossings, thereby substantially amplifying the photon-DP conversion probability.

Using M87 spectral data extending to the LOFAR band, we obtain $\epsilon \sim 7 \times 10^{-6}$ at $m_{A'} \sim 5 \times 10^{-7}$ eV, among the strongest astrophysical limits at this scale. From the Crab SED, we further obtain an even stronger constraint, $\epsilon \simeq 8 \times 10^{-7}$ at $m_{A'} \simeq 4 \times 10^{-9}$ eV for oscillation baselines of order 10^3 km, surpassing existing astrophysical limits in realistic structured plasma backgrounds. While current laboratory and cosmological bounds (e.g., Cavendish-type experiments and COBE/FIRAS limits) remain stronger by one to two orders of magnitude at comparable masses, we emphasize that plasma structuring around extreme objects offers exceptional discovery potential, with clear prospects to outperform laboratory reach in systems with larger surface magnetic fields. In particular, magnetars with surface

magnetic fields as large as $B_0/B_c \sim 1000$ yield projected sensitivities that approach, and in some regions surpass, the strongest current laboratory bounds.

Non-monotonicity may also arise in angular directions, where resonance points can coalesce and the standard LZ treatment breaks down in analogy to the radial case, modifying oscillation probabilities and potentially leaving distinctive spectral signatures. The same formalism can be extended to additional photon frequency bands of M87*, as well as to high-field central engines such as magnetars powering soft gamma repeaters and gamma-ray bursts, where even stronger kinetic-mixing limits are expected from spectral analyses. Similar resonant oscillation effects can also be investigated in other plasma environments, including the intergalactic medium and the solar atmosphere, for realistic non-monotonic profiles.

Beyond photon-DP conversion, structured plasma backgrounds can also affect neutrino flavor oscillations, altering propagation phases and transition probabilities in a plasma parameter-dependent manner. Extensions to angular plasma resonances, multi-band spectral evolution, and plasma-induced modifications of both photon and neutrino oscillations constitute well-motivated future directions. We defer a dedicated analysis of these aspects to forthcoming work.

ACKNOWLEDGMENTS

T.K.P would like to thank Indian Association for the Cultivation of Science (IACS) for their kind hospitality, where this project was initiated. This article is based upon work from the COST Actions “COSMIC WISPers” (CA21106) and “BridgeQG” (CA23130), both supported by COST (European Cooperation in Science and Technology). PS acknowledges support from the University Grants Commission, Government of India, through a Senior Research Fellowship.

- [1] M. Baryakhtar et al., *Dark Matter In Extreme Astrophysical Environments*, in *Snowmass 2021*, 3, 2022 [[2203.07984](#)].
- [2] J. Bramante and N. Raj, *Dark matter in compact stars*, *Phys. Rept.* **1052** (2024) 1 [[2307.14435](#)].

- [3] D.J.E. Marsh, *Axion Cosmology*, *Phys. Rept.* **643** (2016) 1 [[1510.07633](#)].
- [4] P. Carenza, M. Giannotti, J. Isern, A. Mirizzi and O. Straniero, *Axion astrophysics*, *Phys. Rept.* **1117** (2025) 1 [[2411.02492](#)].
- [5] A. Caputo and G. Raffelt, *Astrophysical Axion Bounds: The 2024 Edition*, *PoS COSMICWISPers* (2024) 041 [[2401.13728](#)].
- [6] L. Hui, J.P. Ostriker, S. Tremaine and E. Witten, *Ultralight scalars as cosmological dark matter*, *Phys. Rev. D* **95** (2017) 043541 [[1610.08297](#)].
- [7] T.K. Poddar and A. Dighe, *Constraining electromagnetic couplings of ultralight scalars from compact stars*, [2501.02286](#).
- [8] M. Fabbrichesi, E. Gabrielli and G. Lanfranchi, *The Dark Photon*, [2005.01515](#).
- [9] A. Caputo, H. Liu, S. Mishra-Sharma and J.T. Ruderman, *Modeling Dark Photon Oscillations in Our Inhomogeneous Universe*, *Phys. Rev. D* **102** (2020) 103533 [[2004.06733](#)].
- [10] H. An, M. Pospelov and J. Pradler, *New stellar constraints on dark photons*, *Phys. Lett. B* **725** (2013) 190 [[1302.3884](#)].
- [11] J.H. Zink and M.E. Ramirez-Quezada, *Exploring the dark sectors via the cooling of white dwarfs*, *Phys. Rev. D* **108** (2023) 043014 [[2306.00517](#)].
- [12] Y. Hochberg, B. von Krosigk, E. Kuflik and T.C. Yu, *Impact of Dark Compton Scattering on Direct Dark Matter Absorption Searches*, *Phys. Rev. Lett.* **128** (2022) 191801 [[2109.08168](#)].
- [13] L. Su, L. Wu and B. Zhu, *Probing for an ultralight dark photon from inverse Compton-like scattering*, *Phys. Rev. D* **105** (2022) 055021 [[2105.06326](#)].
- [14] P. Tantirangsri, D. Samart and C. Pongkitivanichkul, *Dark photon Bremsstrahlung and ultra-high-energy cosmic ray*, *Phys. Dark Univ.* **44** (2024) 101432 [[2301.11122](#)].
- [15] B. Holdom, *Searching for ϵ Charges and a New $U(1)$* , *Phys. Lett. B* **178** (1986) 65.
- [16] G. Aldazabal, L.E. Ibanez, F. Quevedo and A.M. Uranga, *D-branes at singularities: A Bottom up approach to the string embedding of the standard model*, *JHEP* **08** (2000) 002 [[hep-th/0005067](#)].
- [17] B. Batell and T. Gherghetta, *Localized $U(1)$ gauge fields, millicharged particles, and holography*, *Phys. Rev. D* **73** (2006) 045016 [[hep-ph/0512356](#)].
- [18] S.A. Abel, M.D. Goodsell, J. Jaeckel, V.V. Khoze and A. Ringwald, *Kinetic Mixing of the Photon with Hidden $U(1)$ s in String Phenomenology*, *JHEP* **07** (2008) 124 [[0803.1449](#)].

[19] B.S. Acharya, S.A.R. Ellis, G.L. Kane, B.D. Nelson and M.J. Perry, *The lightest visible-sector supersymmetric particle is likely to be unstable*, *Phys. Rev. Lett.* **117** (2016) 181802 [[1604.05320](#)].

[20] B.S. Acharya, S.A.R. Ellis, G.L. Kane, B.D. Nelson and M. Perry, *Categorisation and Detection of Dark Matter Candidates from String/M-theory Hidden Sectors*, *JHEP* **09** (2018) 130 [[1707.04530](#)].

[21] T. Gherghetta, J. Kersten, K. Olive and M. Pospelov, *Evaluating the price of tiny kinetic mixing*, *Phys. Rev. D* **100** (2019) 095001 [[1909.00696](#)].

[22] S. Heeba and F. Kahlhoefer, *Probing the freeze-in mechanism in dark matter models with $U(1)'$ gauge extensions*, *Phys. Rev. D* **101** (2020) 035043 [[1908.09834](#)].

[23] B. Díaz Sáez, *Thermal dark photon dark matter, coscattering, and long-lived ALPs*, *Phys. Dark Univ.* **48** (2025) 101852 [[2405.06113](#)].

[24] H.-Y. Zhang, P. Arias, A. Cheek, E.D. Schiappacasse, L. Visinelli and L. Roszkowski, *Dark photon dark matter from flattened axion potentials*, *JHEP* **10** (2025) 142 [[2507.20484](#)].

[25] G. Arsenadze, A. Caputo, X. Gan, H. Liu and J.T. Ruderman, *Shaping dark photon spectral distortions*, *JHEP* **03** (2025) 018 [[2409.12940](#)].

[26] J.L. Feng, M. Toman and E. Welch, *Spin Correlations in Dark Photon Searches*, [2508.18352](#).

[27] R. Lasenby and K. Van Tilburg, *Dark photons in the solar basin*, *Phys. Rev. D* **104** (2021) 023020 [[2008.08594](#)].

[28] J.I. Kapusta and C. Gale, *Finite-temperature field theory: Principles and applications*, Cambridge Monographs on Mathematical Physics, Cambridge University Press (2011), [10.1017/CBO9780511535130](#).

[29] W. Heisenberg and H. Euler, *Consequences of Dirac's theory of positrons*, *Z. Phys.* **98** (1936) 714 [[physics/0605038](#)].

[30] J.L. Feng, J. Smolinsky and P. Tanedo, *Dark Photons from the Center of the Earth: Smoking-Gun Signals of Dark Matter*, *Phys. Rev. D* **93** (2016) 015014 [[1509.07525](#)].

[31] A. Berlin, J.A. Dror, X. Gan and J.T. Ruderman, *Millicharged relics reveal massless dark photons*, *JHEP* **05** (2023) 046 [[2211.05139](#)].

[32] A. Berlin, R. Tito D'Agnolo, S.A.R. Ellis and J.I. Radkovski, *Signals of millicharged dark matter in light-shining-through-wall experiments*, *JHEP* **08** (2023) 017 [[2305.05684](#)].

- [33] C. Zener, *Nonadiabatic crossing of energy levels*, *Proc. Roy. Soc. Lond. A* **137** (1932) 696.
- [34] L.D. Landau, *A theory of energy transfer. 2.*, *Phys. Z. Sowjetunion* **2** (1932) .
- [35] N. Brahma, A. Berlin and K. Schutz, *Photon-dark photon conversion with multiple level crossings*, *Phys. Rev. D* **108** (2023) 095045 [[2308.08586](https://arxiv.org/abs/2308.08586)].
- [36] A. Caputo, A.J. Millar, C.A.J. O'Hare and E. Vitagliano, *Dark photon limits: A handbook*, *Phys. Rev. D* **104** (2021) 095029 [[2105.04565](https://arxiv.org/abs/2105.04565)].
- [37] C. O'Hare, “cajohare/axionlimits: Axionlimits.” <https://cajohare.github.io/AxionLimits/>, July, 2020. 10.5281/zenodo.3932430.
- [38] J. Jaeckel and S. Roy, *Spectroscopy as a test of Coulomb’s law: A Probe of the hidden sector*, *Phys. Rev. D* **82** (2010) 125020 [[1008.3536](https://arxiv.org/abs/1008.3536)].
- [39] D. Kroff and P.C. Malta, *Constraining hidden photons via atomic force microscope measurements and the Plimpton-Lawton experiment*, *Phys. Rev. D* **102** (2020) 095015 [[2008.02209](https://arxiv.org/abs/2008.02209)].
- [40] R. Povey, J. Hartnett and M. Tobar, *Microwave cavity light shining through a wall optimization and experiment*, *Phys. Rev. D* **82** (2010) 052003 [[1003.0964](https://arxiv.org/abs/1003.0964)].
- [41] T. O’Shea, M. Giannotti, I.G. Irastorza, L.M. Plasencia, J. Redondo, J. Ruz et al., *Prospects on the detection of solar dark photons by the International Axion Observatory*, *JCAP* **06** (2024) 070 [[2312.10150](https://arxiv.org/abs/2312.10150)].
- [42] J. Redondo, *Helioscope Bounds on Hidden Sector Photons*, *JCAP* **07** (2008) 008 [[0801.1527](https://arxiv.org/abs/0801.1527)].
- [43] V. Cardoso, O.J.C. Dias, G.S. Hartnett, M. Middleton, P. Pani and J.E. Santos, *Constraining the mass of dark photons and axion-like particles through black-hole superradiance*, *JCAP* **03** (2018) 043 [[1801.01420](https://arxiv.org/abs/1801.01420)].
- [44] M. Danilov, S. Demidov and D. Gorbunov, *Constraints on hidden photons produced in nuclear reactors*, *Phys. Rev. Lett.* **122** (2019) 041801 [[1804.10777](https://arxiv.org/abs/1804.10777)].
- [45] J. Chluba, B. Cyr and M.C. Johnson, *Revisiting dark photon constraints from CMB spectral distortions*, *Mon. Not. Roy. Astron. Soc.* **535** (2024) 1874 [[2409.12115](https://arxiv.org/abs/2409.12115)].
- [46] F. McCarthy, D. Pirvu, J.C. Hill, J. Huang, M.C. Johnson and K.K. Rogers, *Dark Photon Limits from Patchy Dark Screening of the Cosmic Microwave Background*, *Phys. Rev. Lett.* **133** (2024) 141003 [[2406.02546](https://arxiv.org/abs/2406.02546)].

[47] N. Vinyoles, A. Serenelli, F.L. Villante, S. Basu, J. Redondo and J. Isern, *New axion and hidden photon constraints from a solar data global fit*, *JCAP* **10** (2015) 015 [[1501.01639](https://arxiv.org/abs/1501.01639)].

[48] E. Fischbach, H. Kloor, R.A. Langel, A.T.Y. Liu and M. Peredo, *New geomagnetic limits on the photon mass and on long range forces coexisting with electromagnetism*, *Phys. Rev. Lett.* **73** (1994) 514.

[49] S. Yan, L. Li and J. Fan, *Constraints on photon mass and dark photon from the Jovian magnetic field*, *JHEP* **06** (2024) 028 [[2312.06746](https://arxiv.org/abs/2312.06746)].

[50] D.K. Hong, C.S. Shin and S. Yun, *Cooling of young neutron stars and dark gauge bosons*, *Phys. Rev. D* **103** (2021) 123031 [[2012.05427](https://arxiv.org/abs/2012.05427)].

[51] S.-P. Li and X.-J. Xu, *Production rates of dark photons and Z' in the Sun and stellar cooling bounds*, *JCAP* **09** (2023) 009 [[2304.12907](https://arxiv.org/abs/2304.12907)].

[52] P. Arias, D. Cadamuro, M. Goodsell, J. Jaeckel, J. Redondo and A. Ringwald, *WISPy Cold Dark Matter*, *JCAP* **06** (2012) 013 [[1201.5902](https://arxiv.org/abs/1201.5902)].

[53] S.D. McDermott and S.J. Witte, *Cosmological evolution of light dark photon dark matter*, *Phys. Rev. D* **101** (2020) 063030 [[1911.05086](https://arxiv.org/abs/1911.05086)].

[54] S.J. Witte, S. Rosauro-Alcaraz, S.D. McDermott and V. Poulin, *Dark photon dark matter in the presence of inhomogeneous structure*, *JHEP* **06** (2020) 132 [[2003.13698](https://arxiv.org/abs/2003.13698)].

[55] A. Caputo, H. Liu, S. Mishra-Sharma and J.T. Ruderman, *Dark Photon Oscillations in Our Inhomogeneous Universe*, *Phys. Rev. Lett.* **125** (2020) 221303 [[2002.05165](https://arxiv.org/abs/2002.05165)].

[56] A. Basu, R. Beck, P. Schmidt and S. Roy, *Synchrotron spectral index and interstellar medium densities of star-forming galaxies*, *Monthly Notices of the Royal Astronomical Society* **449** (2015) 3879
[\[https://academic.oup.com/mnras/article-pdf/449/4/3879/18505476/stv510.pdf\]](https://academic.oup.com/mnras/article-pdf/449/4/3879/18505476/stv510.pdf).

[57] V. Heesen, E. Buie II, C.J. Huff, L.A. Perez, J.G. Woolsey, D.A. Rafferty et al., *Calibrating the relation of low-frequency radio continuum to star formation rate at 1 kpc scale with lofar*, *Astronomy & Astrophysics* **622** (2019) A8.

[58] S.Y. Braude, O.M. Lebedeva, A.V. Megn, B.P. Ryabov and I.N. Zhouck, *The spectra of discrete radio sources at decametric wavelengths—i*, *Monthly Notices of the Royal Astronomical Society* **143** (1969) 301.

[59] A.H. Bridle and C.R. Purton, *Observations of radio sources at 10.03 mhz.*, *The Astronomical Journal* **73** (1968) 717.

[60] R.S. Roger, C.H. Costain and J.D. Lacey, *Spectral flux densities of radio sources at 22.25 mhz. i., The Astronomical Journal* **74** (1969) 366.

[61] M.R. Viner and W.C. Erickson, *26.3-mhz radio source survey. ii - radio source positions and fluxes, The Astronomical Journal* **80** (1975) 931.

[62] K.I. Kellermann, I.I.K. Pauliny-Toth and P.J.S. Williams, *The Spectra of Radio Sources in the Revised 3c Catalogue, Astrophys. J.* **157** (1969) 1.

[63] A. Wright and R. Otrupcek, *Parke Catalog, 1990, Australia telescope national facility., PKS Catalog (1990)* (1990) 0.

[64] R.A. Laing and J.A. Peacock, *The relation between radio luminosity and spectrum for extended extragalactic radio sources., MNRAS* **190** (1980) 903.

[65] A.M.M. Scaife and G.H. Heald, *A broadband flux scale for low frequency radio telescopes, Mon. Not. Roy. Astron. Soc.* **423** (2012) 30 [[1203.0977](#)].

[66] F. de Gasperin et al., *M87 at metre wavelengths: the LOFAR picture, Astron. Astrophys.* **547** (2012) A56 [[1210.1346](#)].

[67] R. Bühler and R. Blandford, *The surprising Crab pulsar and its nebula: A review, Rept. Prog. Phys.* **77** (2014) 066901 [[1309.7046](#)].

[68] J.F. Macias-Perez, F. Mayet, F.X. Desert and J. Aumont, *Global spectral energy distribution of the Crab Nebula in the prospect of the Planck satellite polarisation calibration, Astrophys. J.* **711** (2010) 417 [[0802.0412](#)].

[69] M. Meyer, D. Horns and H.S. Zechlin, *The Crab Nebula as a standard candle in very high-energy astrophysics, Astron. Astrophys.* **523** (2010) A2 [[1008.4524](#)].

[70] Q. Yuan, P.-F. Yin, X.-F. Wu, X.-J. Bi, S. Liu and B. Zhang, *A statistical model for the γ -ray variability of the Crab nebula, Astrophys. J. Lett.* **730** (2011) L15 [[1012.1395](#)].

[71] G.B. Rybicki and A.P. Lightman, *Radiative processes in astrophysics*, 1979, <https://api.semanticscholar.org/CorpusID:119403227>.

[72] E. Quataert, *A thermal bremsstrahlung model for the quiescent x-ray emission from sagittarius a*, Astrophys. J.* **575** (2002) 855 [[astro-ph/0201395](#)].

[73] F. Yuan and R. Narayan, *Hot Accretion Flows Around Black Holes, Ann. Rev. Astron. Astrophys.* **52** (2014) 529 [[1401.0586](#)].

[74] EVENT HORIZON TELESCOPE collaboration, *First M87 Event Horizon Telescope Results. V. Physical Origin of the Asymmetric Ring, Astrophys. J. Lett.* **875** (2019) L5 [[1906.11242](#)].

[75] S. Roy, P. Sarkar, S. Sau and S. SenGupta, *Exploring axions through the photon ring of a spherically symmetric black hole*, *JCAP* **11** (2023) 099 [[2310.05908](#)].

[76] K. Hada, K. Asada, M. Nakamura and M. Kino, *M 87: a cosmic laboratory for deciphering black hole accretion and jet formation*, *Astron. Astrophys. Rev.* **32** (2024) 5 [[2412.07083](#)].

[77] Z. Zhang, H. Yan, M. Guo and B. Chen, *Shadows of Kerr black holes with a Gaussian-distributed plasma in the polar direction*, *Phys. Rev. D* **107** (2023) 024027 [[2206.04430](#)].

[78] O. Ning and B.R. Safdi, *Leading Axion-Photon Sensitivity with NuSTAR Observations of M82 and M87*, *Phys. Rev. Lett.* **134** (2025) 171003 [[2404.14476](#)].

[79] F. Marinacci et al., *First results from the IllustrisTNG simulations: radio haloes and magnetic fields*, *Mon. Not. Roy. Astron. Soc.* **480** (2018) 5113 [[1707.03396](#)].

[80] A. Pillepich et al., *First results from the TNG50 simulation: the evolution of stellar and gaseous discs across cosmic time*, *Mon. Not. Roy. Astron. Soc.* **490** (2019) 3196 [[1902.05553](#)].

[81] D. Nelson, A. Pillepich, V. Springel, R. Pakmor, R. Weinberger, S. Genel et al., *First Results from the TNG50 Simulation: Galactic outflows driven by supernovae and black hole feedback*, *Mon. Not. Roy. Astron. Soc.* **490** (2019) 3234 [[1902.05554](#)].

[82] M.J. Rees and J.E. Gunn, *The origin of the magnetic field and relativistic particles in the crab nebula*, *Monthly Notices of the Royal Astronomical Society* **167** (1974) 1 [<https://academic.oup.com/mnras/article-pdf/167/1/1/8079729/mnras167-0001.pdf>].

[83] P. Goldreich and W.H. Julian, *Pulsar electrodynamics*, *Astrophys. J.* **157** (1969) 869.

[84] A.M.M. Scaife and G.H. Heald, *A broad-band flux scale for low-frequency radio telescopes*, *MNRAS* **423** (2012) L30 [[1203.0977](#)].

[85] F. de Gasperin et al., *M 87 at metre wavelengths: the LOFAR picture*, *Astronomy & Astrophysics* **547** (2012) A56 [[1210.1346](#)].

[86] J.F. Macías-Pérez, F. Mayet, J. Aumont and F.X. Désert, *Global Spectral Energy Distribution of the Crab Nebula in the Prospect of the Planck Satellite Polarization Calibration*, *Astrophys. J.* **711** (2010) 417 [[0802.0412](#)].

[87] M. Meyer, D. Horns and H.S. Zechlin, *The Crab Nebula as a standard candle in very high-energy astrophysics*, *A&A* **523** (2010) A2 [[1008.4524](#)].

[88] Q. Yuan, P.-F. Yin, X.-F. Wu, X.-J. Bi, S. Liu and B. Zhang, *A Statistical Model for the γ -ray Variability of the Crab Nebula*, *Astrophysics Journal* **730** (2011) L15 [[1012.1395](#)].

[89] H.-S. Zechlin, D. Horns and J. Redondo, *New Constraints on Hidden Photons using Very High Energy Gamma-Rays from the Crab Nebula*, *AIP Conf. Proc.* **1085** (2009) 727 [[0810.5501](#)].

[90] M.J. Dolan, F.J. Hiskens and R.R. Volkas, *Constraining dark photons with self-consistent simulations of globular cluster stars*, *JCAP* **05** (2024) 099 [[2306.13335](#)].

[91] N. Vinyoles, A. Serenelli, F.L. Villante, S. Basu, J. Redondo and J. Isern, *New axion and hidden photon constraints from a solar data global fit*, *JCAP* **2015** (2015) 015 [[1501.01639](#)].

[92] M. Schwarz, E.-A. Knabbe, A. Lindner, J. Redondo, A. Ringwald, M. Schneide et al., *Results from the Solar Hidden Photon Search (SHIPS)*, *JCAP* **08** (2015) 011 [[1502.04490](#)].

[93] A. Romanenko et al., *Search for Dark Photons with Superconducting Radio Frequency Cavities*, *Phys. Rev. Lett.* **130** (2023) 261801 [[2301.11512](#)].

[94] M. Betz, F. Caspers, M. Gasior, M. Thumm and S.W. Rieger, *First results of the CERN Resonant Weakly Interacting sub-eV Particle Search (CROWS)*, *Phys. Rev. D* **88** (2013) 075014 [[1310.8098](#)].